Eur. Phys. J. A **23**, 61–68 (2005)
DOI 10.1140/epja/i2004-10031-y

THE EUROPEAN PHYSICAL JOURNAL A

Spallation neutron spectrum on a massive lead/paraffin target irradiated with 1 GeV protons

J. Adam[1,a], A.R. Balabekyan[1], V.S. Barashenkov[1], R. Brandt[4], V.M. Golovatiouk[1], V.G. Kalinnikov[1], K. Katovsky[1,b], M.I. Krivopustov[1], V. Kumar[2], H. Kumawat[1,2,c], R. Odoj[3], V.S. Pronskikh[1], A.A. Solnyshkin[1], V.I. Stegailov[1], V.M. Tsoupko-Sitnikov[1], and W. Westmeier[4]

[1] Joint Institute for Nuclear Research (JINR), Dubna, 141980, Russia
[2] HENP Laboratory, Physics Department, University of Rajasthan, Jaipur - 302004, India
[3] Forschungszentrum Jülich (FZJ), 52425 Jülich, Germany
[4] Fachbereich Chemie, Philipps University, 35032 Marburg, Germany

Received: 24 March 2004 / Revised version: 17 September 2004 /
Published online: 29 November 2004 –
Communicated by Th. Walcher

Abstract. The gamma-ray spectra emitted by decaying of residual nuclei produced by spallation neutrons in (n, xn), (n, xnyp), (n, p), (n, γ) reactions with activation threshold detectors, *i.e.* ^{209}Bi, ^{197}Au, ^{59}Co, ^{115}In, ^{232}Th, were measured in the Laboratory of Nuclear Problems (LNP), JINR, Dubna, Russia. Spallation neutrons were generated by bombarding a 20 cm long cylindrical lead target with 8 cm diameter surrounded by a 6 cm thick layer of paraffin moderator with 1 GeV proton beam from the NUCLOTRON accelerator. Reaction rates and a spallation neutron spectrum were measured and compared with CASCADE code calculations.

PACS. 28.41.Kw Radioactive wastes, waste disposal – 29.30.Kv X- and γ-ray spectroscopy – 02.70.Uu Applications of Monte Carlo methods – 07.05.Fb Design of experiments

1 Introduction

In the last decade, Accelerator-Driven sub-critical Systems (ADS), [1,2] and references therein, where an accelerator is coupled with a reactor, have been considered as a promising and challenging task for transmutation of long-lived radioactive waste and energy production. This system is significantly safer, due to its sub-criticality, than conventional critical reactors. Spallation neutrons are generated by bombardment of heavy targets such as Pb, Pb-Bi (eutectic), Hg etc. with protons and react with fuel material (Th, U etc.) or with exposed radioactive waste from conventional reactors or weapons. For the design of ADS it is important to study neutron spectra and details of nuclear reactions induced by neutrons. Many experimental results are available for thin targets, *e.g.* [3], but for massive targets additional studies of neutron spectra and cross-section are needed for the design of real ADS and to improve the transport codes.

When using thorium as a nuclear ADS fuel the study of the production of problematic transthorium nuclides is essential. There are a few experimental neutron production cross-sections available for thorium, however, some results are in contradiction [4,5]. Therefore in a side experiment we also irradiated some Th-metal with primary spallation neutrons.

Some recent experimental results [3] for thin targets obtained by the group of Yu.V. Trebukhovsky on double differential neutron production cross-sections for different targets and comparison with CASCADE, CEM97 and LAHET simulation codes show that calculated neutron multiplicity values are somewhat higher than experimental values, in particular at small angles. From this point of view it may be important to study spallation neutron spectra (spatial and energy distribution) as well as total neutron yields in order to improve the physics implemented in simulation codes.

2 Experimental setup and method of measurements

The sketched setup of the GAMMA-2 experiment is given in fig. 1. A target consisting of 20 lead discs, each of 1 cm

[a] On leave from Nuclear Physics Institute CAS Řež, 25068, Czech Republic.
[b] On leave from Czech Technical University, Prague, 18000, Czech Republic.
[c] e-mail: kumawat@jinr.ru; kumawat77@yahoo.com

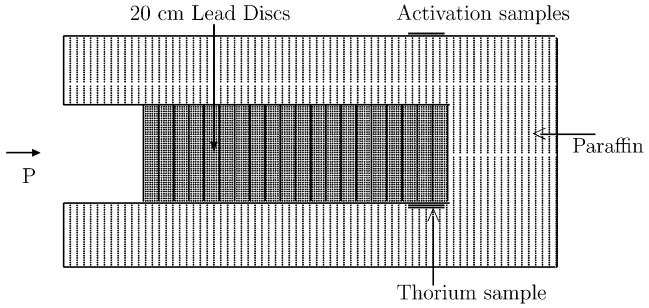

Fig. 1. The experimental setup with lead target and paraffin moderator.

Table 1. Characteristics of the irradiated samples.

Target	Mass (g)	Thickness (g/cm^2)	Thickness (mm)
^{209}Bi	3.1	2.44	2.50
^{179}Au	1.19	1.06	0.55
^{115}In	0.11	0.07	0.09
^{59}Co	3.33	3.56	4.0
^{232}Th	0.013	0.0018	0.0046

thickness and 8 cm diameter and surrounded by 6 cm paraffin moderator was irradiated by a 1 GeV proton beam extracted from the Nuclotron in the Laboratory of High Energies (LHE) at JINR for 5 hours and 29 minutes. Activation samples of ^{209}Bi, ^{197}Au, ^{59}Co, ^{115}In were placed on the top of the paraffin surface as shown in fig. 1. A ^{232}Th sample wrapped in thin aluminium was placed directly on the surface of the lead target inside the paraffin. The ^{232}Th sample was prepared by the Bhaba Atomic Research Center (Mumbai, India) and the other samples were supplied by the University of Rajasthan and LNP. The physical characteristics of these samples are given in table 1.

The proton beam was monitored by thin Al foils situated approximately 60 cm before the target to avoid the influence of backwards-emitted neutrons produced from the target. The intensity of protons was obtained with the ^{27}Al(p, 3pn)^{24}Na reaction using a cross-section of 10.51(17) mb [6] (the uncertainty in brackets refers to the last digit). The influence of the ^{27}Al(n, α)^{24}Na reaction was not taken into account as it is negligible under the experimental conditions [7]. The variation of the beam intensity during irradiation is presented in fig. 2. It is clear from fig. 2 that the assumption of a constant intensity is not justified when calculating the decay of products during irradiation. We have taken into account the correction for the fluctuation and interruption of the beam. This correction was done for all the product nuclei, which is particularly important for product nuclei having a half-life shorter than the irradiation time (for example, the correction to ^{201}Bi ($T_{1/2}$ = 108 min) was 25%). The proton flux on the lead target was determined as 10.90(65)10^8 protons/s as determined by the monitoring reaction ^{27}Al(p, 3pn)^{24}Na taking into account the beam fluctuations and coincidence summing.

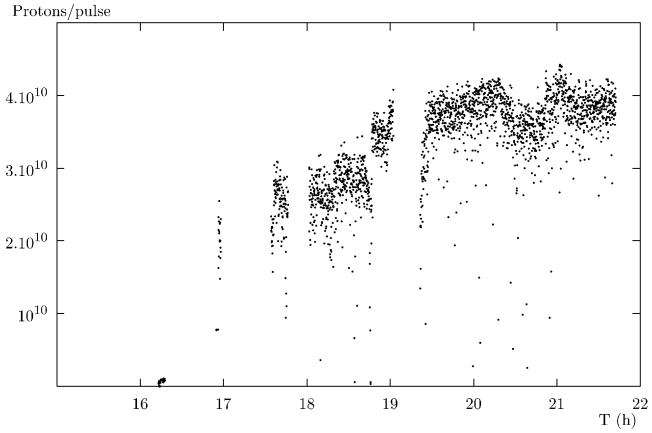

Fig. 2. Variation of the beam intensity during irradiation. Each dot shows one pulse of particular intensity.

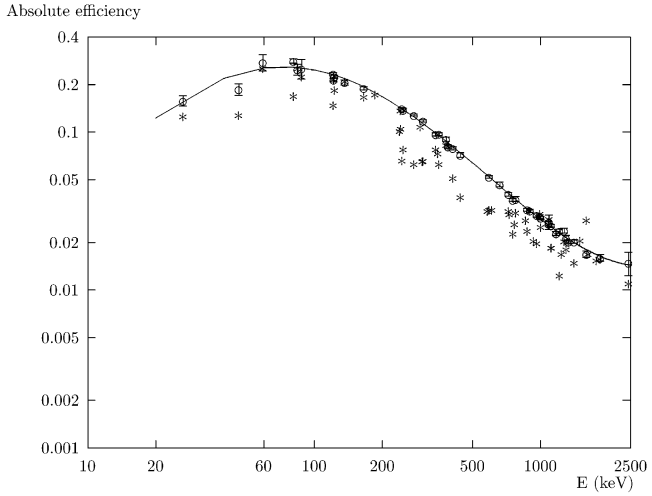

Fig. 3. Absolute efficiency at 0 cm distance and least-squares fit. Asterisks (∗) are raw data and circles (∘) are data after coincidence summing correction.

Measurements of the spectra of gamma-rays emitted by the above-mentioned samples were started at LNP 3 hours after the irradiation and 11-12 spectra from each sample were measured with time intervals up to 15 days after the irradiation. The measurement of spectra from the thorium sample was started 19 hours after the irradiation and measured up to one month with appropriate time intervals. Samples irradiated by spallation neutrons were measured by a High-Purity Germanium (HPGe) detector with 28% relative efficiency and an energy resolution of 2 keV (FWHM ^{60}Co at 1332 keV) at LNP. Due to the low activity in the samples, we measured at 0 cm distance from the detector endcap. Recording of gamma-ray spectra was carried out with a high-rate multichannel buffer SPECTRUM MASTER 921.

The DEIMOS Program [8] was used in an interactive mode for spectrum analysis. This program determined the areas and positions of peaks taking into account the background level. Exact energies of the peaks were found using

Table 2. Experimental and calculated reaction rates for ^{209}Bi sample.

Target/Product	$E_{\rm th}$ (MeV)	$T_{1/2}$	E_γ (keV)	I_γ (%)	$R_i^{\rm cal}$ (10^{-29}) ($\rm p^{-1}\cdot atom^{-1}$)	$R_i^{\rm expt}$ (10^{-29}) ($\rm p^{-1}\cdot atom^{-1}$)	Uncertainty (±%)
^{209}Bi (n, 4n)^{206}Bi	22.55	6.243 d	803.1	98.9	5.28	6.77	7
			881.01	66.16		6.82	8
						6.79[a]	7
^{209}Bi(n, 5n)^{205}Bi	29.62	15.31 d	703.4	31.0	3.00	4.46	8
			1764.3	32.47		3.94	10
						4.26[a]	7
^{209}Bi(n, 6n)^{204}Bi	38.13	11.30 h	899.2	99.2	1.48	2.82	9
			983.98	58.76		1.87	10
						2.40[a]	8
^{209}Bi(n, 7n)^{203}Bi	45.37	11.76 h	820.5	29.7	1.15	2.33	8
			825.2	14.6		2.54	12
						2.38[a]	7
^{209}Bi(n, 9n)^{201}Bi	61.69	1.8 h	629.1	24.0	0.48	0.91	19

[a] Weighted average value.

Table 3. Experimental and calculated reaction rates for ^{197}Au sample.

Target/Product	$E_{\rm th}$ (MeV)	$T_{1/2}$	E_γ (keV)	I_γ (%)	$R_i^{\rm cal}$ (10^{-29}) ($\rm p^{-1}\cdot atom^{-1}$)	$R_i^{\rm expt}$ (10^{-29}) ($\rm p^{-1}\cdot atom^{-1}$)	Uncertainty (±%)
^{197}Au(n, 2n)^{196}Au	8.113	6.183 d	355.73	87	8.58	10.3	6
			333.03	22.9		10.0	7
						10.1[a]	5
^{197}Au(n, 4n)^{194}Au	23.205	38.02 h	328.4	60	4.77	5.1	7
^{197}Au(n, 6n)^{192}Au	38.939	4.94 h	296.0	22.3	2.35	3.0	15
			316.5	58.0		2.3	10
						2.5[a]	9
^{197}Au(n, 7n)^{191}Au	45.97	3.18 h	586.5	17	1.21	1.7	8
^{197}Au(n, γ)^{198}Au		2.695 d	411.80	95.5		1382	5
			675.88	0.8		1386	7
						1383[a]	5

[a] Weighted average value.

suitable calibration points. The program also gave a tentative list of product isotopes using a rich library (containing energy, intensity per decay and half-life of the isotopes).

After spectrum handling, the data were cleaned from the internal and external background lines. The corrected intensities of the gamma lines were used to determine the half-lives of the product nuclei, including complex lines. Identification of the products was based on the energies and intensities of the gamma lines as well as half-lives as given in Atomic Data and Nuclear Data Tables [9,10]. The reaction rates R in units of (proton $^{-1}\cdot$ atom^{-1}) of product nuclei were calculated taking into account the corrections for peak efficiency of the HPGe detector, for coincidence summing effect, for self-absorption and for decay during irradiation (with consideration of the fluctuation of beam current during the irradiation).

The reaction rate R (proton $^{-1}\cdot$ atom^{-1}) is related to the neutron flux as follows [11]:

$$R = \int_{E_{\rm th}}^{\infty} \sigma(E) \cdot \phi(E) \cdot {\rm d}E \; . \qquad (1)$$

Here, $\phi(E)$ is neutron flux (neutron/(cm$^2\cdot$ MeV $\cdot$ proton)) passing through the samples, $E_{\rm th}$ is the threshold neutron energy for the observed reaction in the particular sample.

We have measured the efficiency of the detector at 0 cm and 25 cm distance from the detector using calibrated sources of ^{137}Cs, ^{109}Cd, ^{139}Ce, ^{88}Y, ^{113}Sn, ^{152}Eu, ^{154}Eu, ^{228}Th, ^{241}Am, ^{54}Mn, ^{60}Co and applied the corresponding

Table 4. Experimental and calculated reaction rates for ^{59}Co sample.

Target/Product	$E_{\rm th}$ (MeV)	$T_{1/2}$	E_γ (keV)	I_γ (%)	$R_i^{\rm cal}$ (10^{-29})	$R_i^{\rm expt}$ (10^{-29})	Uncertainty (±%)
^{59}Co(n, 2n)^{58}Co	10.64	70.82 d	810.75	99.45	6.45	5.9	7
^{59}Co(n, 3n)^{57}Co	19.37	271.79 d	122.06	85.5	3.15	1.0	7
			136.47	10.68		1.2	13
						1.0[a]	6
^{59}Co(n, 4n)^{56}Co	30.96	77.27 d	846.75	99.9	0.11	0.36	11
			1238.3	66.95		0.34	17
						0.35[a]	9
^{59}Co(n, 5n)^{55}Co	41.24	17.53 h	931.5	75	.019	0.027	13
^{59}Co (n, p)^{59}Fe	0.796	44.503 d	1099.22	56.5		0.49	9
			1291.56	43.2		0.60	9
						0.55[a]	9
^{59}Co(n, 2p6n)^{52}Mn	67.8	5.591 d	1434.09	100.0		0.14	8
			935.54	94.9		0.12	8
						0.13[a]	8

([a]) Weighted average value.

Table 5. Experimental and calculated reaction rates for ^{115}In and ^{232}Th samples.

Target/Product	$E_{\rm th}$ (MeV)	$T_{1/2}$	E_γ (keV)	I_γ (%)	$R_i^{\rm cal}$ (10^{-29}) ($p^{-1}\cdot$ atom^{-1})	$R_i^{\rm expt}$ (10^{-29}) ($p^{-1}\cdot$ atom^{-1})	Uncertainty (±%)
^{115}In(n, 5n)^{111}In	33.74	2.8047 d	171.4	90.24	2.06	2.4	9
			245.35	94.0		2.2	8
						2.3[a]	7
^{115}In(n, 6n)^{110}In	43.82	4.9 h	657.75	98.29	0.48	0.79	16
^{115}In(n, 7n)^{109}In	51.96	4.2 h	203.5	73.5	0.32	0.76	13
^{232}Th (n, γ)^{233}Th[b]		26.967 d	300.12	06.6		2963	9
			311.98	38.6		3209	6
						3133[a]	5

([a]) Weighted average value.
([b]) We observed ^{233}Pa as decay daughter of primary product ^{233}Th.

coincidence summing corrections, neglecting coincidence summing at 25 cm. The curve for absolute efficiency at sample 0 cm distance with and without coincidence summing correction is shown in fig. 3. We have taken into account the correction for all observed product nuclei following [12]. Corrections were up to 40% (*e.g.* ^{204}Bi) for such close geometry.

3 Modelling and discussion

The experimental reaction rates are compared with values calculated by the CASCADE [13] code in tables 2-5, where $E_{\rm th}$ is the threshold energy, E_γ is the observed gamma-ray energy, I_γ is the emission rate (intensity) of this gamma-ray per decay , $T_{1/2}$ is the half-life of the produced nuclei, $R_i^{\rm calc}$ is the calculated reaction rate for the i-th reaction by the CASCADE code and $R_i^{\rm exp}$ the experimental reaction rate.

Uncertainties in the tables are calculated from the statistical error of the spectral data plus the 6% uncertainty of the beam intensity measured via the ^{27}Al(p, 3pn)^{24}Na monitor reaction. The weighted average reaction rates are presented in case that two or three lines were observed from the same nuclide. For calculating the average only statistical uncertainties have been taken into account.

Model calculations were performed by Monte Carlo simulation, using the CASCADE code [13] to obtain the theoretical spallation neutron spectra and reaction rates (other calculations were published [14] using the same code for the above-mentioned setup, where one can find more details about the spatial and energy spectra of the

neutrons). The spectrum presented in this paper is at the position of the samples (which were situated at the same distance in circular form around the paraffin surface, as shown in fig. 1). The spectrum is not at the surface of the lead but after the paraffin. Paraffin $(CH_2)_n$ with density 0.87 g/cm^3 was considered in the CASCADE code calculations.

The code realised the particle transport in three stages: 1) sampling of particle (ion) mean free path in the medium taking into account the energy loss of a charged particle and a possible decay of non-stable particles ($\pi^0, \pi^\pm$). All π-mesons are considered to decay into γ-quanta at the point of their creation. The ionization losses of π-mesons, protons and light ions are calculated by Sternheimer's method [15]. In the lower-energy region Lindhard's approach [16] is used and a semi-phenomenological procedure [17] is applied for the heavy ions.

2) Simulation of the particle interaction with a nucleus is considered along its path. In case of inelastic interaction the CASCADE code considers three stages of reactions for calculation: a) intranuclear cascade stage, originally developed at Dubna: In this part of the calculation, primary particles can be re-scattered and they may produce secondary particles several times prior to absorption or escape from the target. b) Pre-equilibrium stage: In this part of the reaction, relaxation of the nuclear excitation is treated according to the exciton model of the pre-equilibrium decay. Proton, neutron, deuterium, tritium, ^{3}He and ^{4}He are considered as emitted particles in the pre-equilibrium and in the subsequent equilibrium stage. c) Equilibrium stage: This part considers the particle evaporation/fission of the thermally equilibrated nucleus. The properties of the elastically scattered high-energy particles are considered by means of plainclothesman formulae.

3) This stage considers the transport of neutrons. The code uses 26-group constants [18] for neutron transport cross-sections below 10.5 MeV. The neutrons can moderate by numerous elastic collisions, can make fission in case of fissile material and finally can be captured in the (n, γ) reaction. It was assumed that the cascade particle is stopped if its energy is less than the boundary energy E_b which equals 2 MeV for $\pi^\pm$, 10 MeV for proton and deutron, 30 MeV for tritium and 100 MeV for all heavier nuclei. Low-energy π^--mesons are captured in a nucleus creating new intranuclear cascades. Neutrons are traced down to thermalization. The algorithm is cyclical in nature and is reduced to several repetitions of all these possible operations. For more details, see refs. [13,19] and references therein.

We simulated 10^5 cascades (with $< 1\%$ uncertainty in the calculation) to calculate spectra and cross-section for different channels of the reactions. We calculated the probabilities for different reactions (n, xn) and then normalized to the total inelastic cross-section taken from [20,21] and obtained the cross-section. We calculated the cross-section for mono-energetic neutrons (below 50 MeV we calculated the cross-section for each neutron energy with energy interval of 2 MeV and later with 5 MeV energy interval up to 150 MeV and with 20 MeV energy interval for the higher energies). We considered quadratic interpolation to know the cross-section for the energies between these intervals. An example of the cross-section for the ^{209}Bi(n, 4n)^{206}Bi reaction calculated with the CASCADE code and the comparison with the experimental cross-section [11] is given in fig. 4. A similar procedure was adopted to calculate the cross-section by the CASCADE code for all samples. For the calculation of the theoretical reaction rate we used $\mathrm{d}E \approx \Delta E = 2$ MeV for the integration in eq. (1).

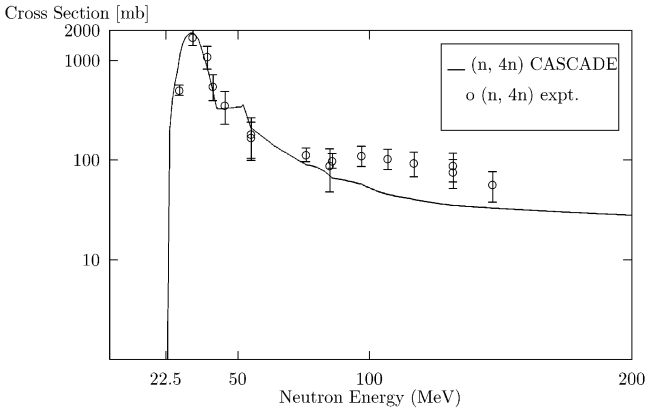

Fig. 4. Comparison of experimental [11] and calculated [13] cross-section for the ^{209}Bi (n, 4n) ^{206}Bi reaction.

One can see from tables 2-5 that the calculated reaction rates below a threshold energy of 30 MeV are 10–30% lower than the experimental reaction rates, but the reaction rates become much lower (up to factor 2) at higher neutron energies. Such a trend was observed for all samples. Although there is a deviation from this trend for Co.

From the ^{232}Th sample we clearly observed ^{233}Pa which is the first daughter of the single-neutron capture product; this finding qualitatively indicates that even directly on the surface of the primary lead target one can find low-energy neutrons abundantly. Of course there must be a higher number of low-energy neutrons on the paraffin surface due to moderation (see more details in ref. [14], where the neutron energy spectrum is presented at the surface of the paraffin and the lead target, supercold neutrons are also shown in tables).

4 Unfolding of neutron spectra

Experimental neutron spectra were deduced using the following procedures: On the right side of eq. (1) there are two energy-dependent variables, *i.e.* the cross-section and the neutron fluence. In a first analysis we assume a constant neutron fluence over some energy and integrate for the cross-section (Analysis ♯1 below) and for the second analysis we follow ref. [22] and consider the cross-section as constant and integrate for the neutron fluence (Analysis ♯2 below).

Analysis ♯1:

The cross-sections of several isotopes produced in a particular sample are taken as references. A constant

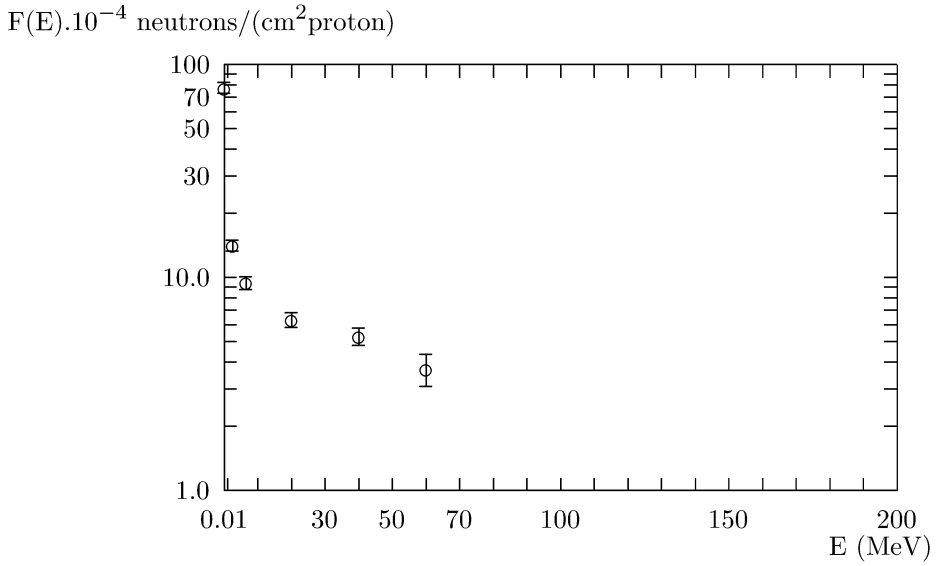

Fig. 5. The integral function $F(E)$ (neutrons/(cm^2 proton)) of neutron spectra calculated for the second analysis method.

neutron fluence is assumed from the threshold energy for the (n, xn) reaction with the highest value of x to the maximum possible energy of neutrons, which is theoretically almost up to the incident proton energy. The maximum neutron energy as calculated by the CASCADE code is only around 600 MeV, however, this difference in the maximum neutron energy affects the calculated spectrum only negligibly because the cross-section for higher neutron energies is very small (see fig. 4, the cross-section of Bi). The fluence from the threshold of the (n, (x−1)n) reaction to the threshold of the (n, xn) reaction is again assumed to be constant and one can calculate that respective part of the spectrum, and so on. In this way one successively reaches the lower-energy end of the spectrum. For example, one obtains the fluence $\phi(9)$ from eqs. (2), (3) and then puts this value into eq. (4) to calculate fluence $\phi(8)$ etc. (see below the method of calculation in eqs. (2)-(5)):

$$R_9^{\rm expt} = \phi(9) \int_{E_{\rm th}({\rm n,9n})}^{E_{\rm max}} \sigma_9(E){\rm d}E \ , \tag{2}$$

$$\phi(9) = \frac{R_9^{\rm expt}}{\int_{E_{\rm th}({\rm n,9n})}^{E_{\rm max}} \sigma_9(E){\rm d}E} \ , \tag{3}$$

$$R_8^{\rm expt} = \phi(8) \int_{E_{\rm th}({\rm n,8n})}^{E_{\rm th}({\rm n,9n})} \sigma_8(E){\rm d}E + \phi(9) \int_{E_{\rm th}({\rm n,9n})}^{E_{\rm max}} \sigma_8(E){\rm d}E \ , \tag{4}$$

$$R_7^{\rm expt} = \phi(7) \int_{E_{\rm th}({\rm n,7n})}^{E_{\rm th}({\rm n,8n})} \sigma_7(E){\rm d}E + \phi(8) \int_{E_{\rm th}({\rm n,8n})}^{E_{\rm th}({\rm n,9n})} \sigma_7(E){\rm d}E + \phi(9) \int_{E_{\rm th}({\rm n,9n})}^{E_{\rm max}} \sigma_7(E){\rm d}E \ . \tag{5}$$

The spectrum above 22.5 MeV has been deduced using experimental cross-section and reaction rates for the Bi sample, from 8.4 to 22.5 MeV the spectrum is obtained using the ^{197}Au (n, 2n)^{196}Au reaction. We used the ^{59}Co (n, p) ^{59}Fe reaction from the 3.5 (though the theoretical neutron energy threshold for this reaction is 0.8 MeV but the experimental threshold is 3.5 MeV) to 8.4 MeV region. Experimental cross-sections for all the reactions are taken from [11,23]. The spectrum obtained in this manner is represented in fig. 6 with a dotted histogram named Analysis ♯1. Errors are shown with vertical error bars.

Analysis ♯2:

A second approach to obtain the spectra is described in ref. [22] where the procedure shall only be presented here for completeness:

$$R_i^{\rm expt} = \sigma_i^{\rm eff} \int_{E_i^{\rm eff}}^{\infty} \phi(E){\rm d}E \ . \tag{6}$$

Here

$$E_i^{\rm eff} = E_i^{\rm th} \ . \tag{7}$$

The neutron fluence $\phi(E)$ to be used in eq. (6) is the theoretical fluence (calculated by the CASCADE code at the place of the samples), all the notations are the same as above. Thus, in this approach one must start from the theoretical neutron spectrum and calculate $\sigma_i^{\rm eff}$, which is the effective cross-section for the particular reaction. In this way one gets a function $F(E_i^{\rm eff})$ as an integral of the theoretical neutron spectrum with the experimental errors in the reaction rates:

$$F(E_i^{\rm eff}) = \frac{R_i^{\rm expt}}{\sigma_i^{\rm eff}} \ , \tag{8}$$

and one can get the general formula as

$$F(E) = \int_E^{\infty} \phi(E'){\rm d}E' \ , \tag{9}$$

$$\phi(E) = -\frac{{\rm d}F(E)}{{\rm d}E} \ . \tag{10}$$

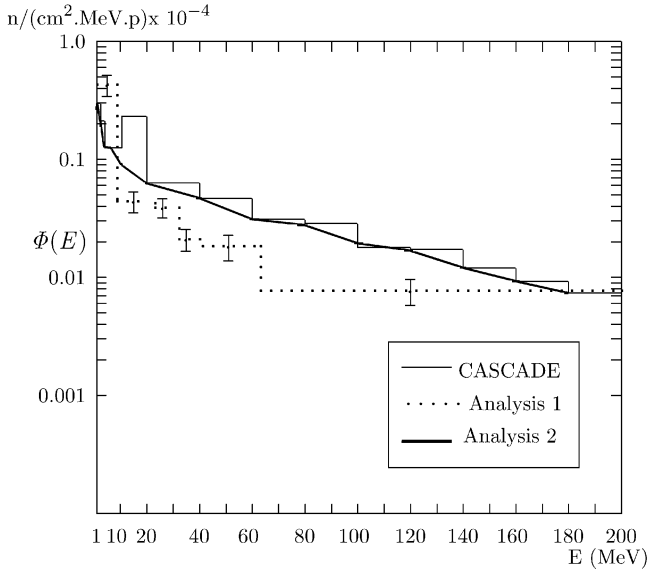

Fig. 6. Comparison of experimentally deduced (by the two analyses) and calculated neutron spectra.

In this second approach one starts with the theoretical neutron fluence to calculate the effective cross-section and later to calculate the integral function $F(E)$ (number of neutrons/(cm^2 proton)) of the neutron fluence. The function $F(E)$ is shown in fig. 5. One can then obtain the "experimental" spectrum by differentiating the integral function $F(E)$. In this way the spectrum will not be really experimental but it is strongly influenced by the initial theoretical fluence or in other words: the differentiation of the integral function will always be in good agreement with the theoretical one (see fig. 6, the continuous thick line represents the spectrum from Analysis ♯2, the errors are the same as in the function $F(E)$ and the thin line histogram shows the spectrum calculated by the CASCADE code). The extrapolated spectrum is shown higher than 62 MeV (the highest threshold reaction observed for Bi, see table 2). In our opinion this method is not viable for the generation of an experimental neutron spectrum and for comparison with theory. We prefer the first analysis method in which the product cross-section is well known with certain experimental uncertainties and the neutron spectrum is completely deduced from the experimental values. A comparison of calculated and deduced neutron fluences obtained by both analyses is given in fig. 6.

5 Conclusions

From the tables 2-5 it is clear that the calculated reaction rates are 10 to 30% lower than the experimental ones for products where the reaction threshold energy $E_{\rm th}$ is in the region of 10 to 30 MeV. In the higher-energy region the calculated rates are lower up to 2 times. As can be seen in fig. 6, the experimental neutron yield is smaller (up to 2-3 times) than the neutron yield calculated by the CASCADE code for energy higher than 10 MeV but slightly lower below 10 MeV. This finding about spectra is in agreement with our previous results [3], where such a discrepancy was also observed for neutrons that were created in proton-Pb collisions at $E = 1$ GeV and 1.6 GeV in thin targets. (It is also important to note that similar disagreement was also observed with some popular codes LAHET, CEM [3]. Some recent comparison of results with different codes, *i.e.* MCNPX (Bertini), MCNPX (CEM), MCNPX (ISABEL) and CASCADE/INPE, has been performed in [24]. From these results one can conclude that all these codes give almost the same results and need further improvements. Unfortunately, we do not have the possibility to compare our results with the other codes.)

However, this finding is different than the reaction rates which are the product of the neutron flux and cross-section. The reason of the disagreement might be that the code overestimates the cross-section slightly near the target mass number, *i.e.* ^{209}Bi (n, 2n)^{206}Bi, and significantly underestimates it for farther mass nuclei (nuclei far from the target mass number), *i.e.* ^{209}Bi (n, 9n)^{201}Bi. The CASCADE code needs improvements for the decay of excited nuclei. Particularly, in the code, the more exact level density formulas [25] and cross-sections for the production of residual nuclei from the evaporation model [26] need to be used. In [27] it is shown that the formula considered in the CASCADE code overestimates the cross-sections for the evaporating particles (see ref. [27] for the details of calculations). Presently the used evaporation model does not distinguish heavy and light nuclei, so it is important to consider the Fermi theory for the decay of lighter nuclei ($Z \leq 13$). The improved CASCADE code results will be published at some point in the future.

The authors are thankful to the Nuclotron Group, LHE, JINR for the irradiation and LNP, JINR for the measurement of the spectra and H.K. is grateful to BRNS(DAE), ILTP (India) and JINR (Russia) for providing him financial support.

References

1. C.D. Bowman *et al.*, Nucl. Instrum. Methods, A **320**, 336 (1992).
2. F. Carminata *et al.*, CERN report CERN/AT/93-47(ET) (1993).
3. Yu. V. Trebukhovsky *et al.*, ITEP-3, 2003; Yad. Fiz. **67**, 1087 (2004).
4. B.D. Kuzminov, V.N. Manokhin, Nucl. Constants **3-4**, 41 (1997).
5. V.N. Manokhin, N. Odano, A. Hasegawa, JAERI - DAta / Code 2001-019.
6. J.B.Cumming, Annu. Rev. Nucl. Sci. **13**, 261 (1963); W. Westmeier *et al.*, private communication.
7. J.-S. Wan *et al.*, Nucl. Instrum. Methods Phys. Res. B **155**, 110 (1999).
8. J. Frana, J. Radioanal. Nucl. Chem. **3-257**, 583 (2003).
9. U. Reus, W. Westmeier, At. Data Nucl. Data Tables **29** (1983).
10. `http://nucleardata.nuclear.lu.se/nucleardata/toi/radSearch.asp`.

11. E. Kim *et al.*, Nucl. Sci. Eng. **129**, 209 (1998).
12. K. Debertin, U. Schotzig, Nucl. Instrum. Methods **158**, 471 (1979).
13. V.S. Barashenkov, Comput. Phys. Commun. **126**, 28 (2000).
14. V.S. Barashenkov, V. Kumar, H. Kumawat, V.A. Lobanova, JINR E9-2003-55; Nucl. Instrum. Methods Phys. Res. B **217**, 352 (2004).
15. R. Sternheimer, Phys. Rev. **145**, 247 (1966); Phys. Rev. B **3**, 3681 (1971).
16. L. Lindhard *et al.*, K. Dan. Vidensk. Selsk. Nat.-Fys. Medd. **33**, 14 (1963).
17. V.S. Barashenkov *et al.*, Phys. Part. Nucl. **24**, 246 (1993).
18. L.P. Abagan, N.O. Bazazjanc, M.N. Nikolaev, A.M. Cybulja. *Groupconstants for reactor and shielding calculations*, Energoatomizdat (in Russian) (Moscow, 1981).
19. V.S. Barashenkov, V.D.Toneev, *Interactioms of high-energy particles and nuclei with nuclei*, Energoatomizdat (in Russian) (Moscow, 1972).
20. V.S. Barashenkov. *Cross-sections of interactionsof particles and nuclei with nuclei* (JINR, Dubna, 1993) (in Russian).
21. V.S. Barashenkov, W. Gudowski, A. Polanski, JINR, E2-99-206.
22. B.A. Martsynkevich *et al.*, JINR, P1-2002-65 (in Russian).
23. `http://www-nds.iaea.org/exfor/`.
24. C.H.M. Broeders, A.Yu. Konobeyev, A.A. Travleev, Kertechnik **69/3**, 99 (2004).
25. A. Gilbert, A.G.W. Cameron, Can. J. Phys. **20**, 1446 (1965).
26. I. Dostrovsky, Z. Fraenkel, G. Friedlander, Phys. Rev. **116**, 683 (1959).
27. `http://arxiv.org/PScache/nucl-th/pdf/0208/0208048.pdf`.